Journal of the Meteorological Society of Japan

EARLY ONLINE RELEASE

The DOI for this manuscript is

DOI:10.2151/jmsj.2025-004

J-STAGE Advance published date: October 21, 2024

The final manuscript after publication will replace the preliminary version at the above DOI once it is available.

Estimation of CO_2 fluxes from Tokyo using a global model and tower observation

Kyohei YAMADA[1]

Yosuke NIWA

Yukio TERAO

Yasunori TOHJIMA

National Institute for Environmental Studies, Tsukuba, Japan

Kazuhiro TSUBOI

Kentaro ISHIJIMA

Meteorological Research Institute, Tsukuba, Japan

and

Shohei MURAYAMA

National Institute of Advanced Industrial Science and Technology (AIST), Tsukuba, Japan

January 1, 2024

----

1) Corresponding author: Kyohei Yamada, National Institute for Environmental Studies, Tsukuba, Onogawa 16-2, Tsukuba, Ibaraki, 305-8506 JAPAN

Email: yamada.kyohei@nies.go.jp

Tel: +81-2-9850-2968

Abstract

Quantifying emissions from megacities is important for reduction of greenhouse gases. We used atmospheric carbon dioxide (CO_2) concentration data obtained at an altitude of around 250 m above the ground on TOKYO SKYTREE (TST; a 634-m-high freestanding broadcasting tower; 35.71°N, 139.81°E), which is located north of central Tokyo, Japan. To use the TST observations for estimating net CO_2 fluxes from Tokyo, a global, high-resolution simulation of atmospheric CO_2 transport with CO_2 flux data from a global inverse analysis was performed. In the simulation, atmospheric CO_2 variations were well reproduced at remote sites around Japan. The application of tagged tracers in the simulation revealed that variations of CO_2 concentrations at TST were largely driven by fluxes in the southwest region of Tokyo, including the western Tokyo Bay area where huge power plants are located. Then, we performed a regression analysis of modeled and observed Tokyo-originated CO_2 concentrations, both of which were derived from the simulated background concentrations, while changing the minimum wind speed used in the analysis. The removal of low wind speeds altered the slope of the regression line, and excluding wind speeds below 7 m s^{-1} resulted in a stabilized slope of 0.93 ± 0.08. This stabilized regression indicated that the annual net CO_2 emission from Tokyo is 79.5 ± 6.6 Tg-C $year^{-1}$. Our findings demonstrate that analysis using a global high-resolution model with tagged tracers has the potential to monitor emissions changes in a megacity.

Keywords carbon dioxide; model simulation; East Asia

1. Introduction

The aim of the Paris Agreement in 2015 was to bring about large reductions in the emissions of greenhouse gases (GHGs) to achieve the target of limiting global warming to 1.5/2.0 °C. The cause of the growth of atmospheric concentrations of carbon dioxide (CO_2), one of the most important GHGs, is anthropogenic CO_2 emissions; 81%–91% of which are from fossil-fuel combustion (IPCC, 2022). Urban areas account for 75% of global fossil-fuel emissions; in addition, 55% of the global population lived in urban areas in 2018. This proportion will increase to 60% by 2030, at which time one in three people are expected to live in urban areas with a population of half a million or more (World Bank, 2010; UN Population Division, 2018). So-called "bottom-up" approaches, in which the total emissions from each source category are calculated by means of multiplying activity data by GHG emission factors, are useful for estimating detailed GHG emissions data for different sectors and fuel types. However, there are uncertainties in the assessment of data at an urban scale, due to several factors such as the measurement technique used and data availability (Arioli et al., 2020). Conversely, estimation methods using atmospheric GHG observations and atmospheric transport models to estimate surface fluxes with quantifiable uncertainties are referred to as "top-down" approaches (e.g., Turnbull et al., 2015). For assessing urban emissions by means of a top-down approach, continuous observations of atmospheric GHG concentrations at tall towers are useful because they capture representative signals from emissions.

Tower GHG monitoring networks such as the Indianapolis Flux Experiment (INFLUX; Lauvaux et al., 2016) are being deployed in some urban areas to assess urban GHG emissions. Turnbull et al. (2015) estimated urban CO_2 emissions from Indianapolis using flask sampling data from the INFLUX towers. The urban emissions were estimated from the difference in CO_2 concentrations measured at upwind and downwind sides of the urban area. Miles et al. (2021) also estimated urban CO_2 emissions using observation data from INFLUX towers situated in different vegetation types. Although these multiple tower methods enable estimation of urban emissions based on in situ observations, they are limited in that they require data for a specific wind direction and assume an ideal condition that ignores vertical or horizontal mixing, which would induce concentration changes at the boundaries of the target area.

Tokyo, Japan, is one of the largest cities in the world, with a population of over 37 million as of 2018 (UN Population Division, 2018). Tokyo's main CO_2 emissions are from power generation, automobiles, and industry (Long and Yoshida, 2018). Sun et al. (2021) compared with the capitals of neighboring countries, and they showed that CO_2 emissions from the Tokyo metropolitan area are slightly larger than those of Seoul (South Korea) and half those of Beijing (China). However, the spatial distribution of emissions is centralized, and 90% of CO_2 emissions are concentrated on 56% of the land area. The mean flux from Tokyo is less than half that from Seoul. Especially along the shores of Tokyo Bay, there are large point sources such as power plants and steel plants (Ohyama et al., 2023). In residential areas, fossil-fuel CO_2 emissions come from household gas consumption and traffic emissions (Hirano et al. 2015). Another important factor is inflow from East Asia, where large emissions are produced. Shirai et al. (2012) analyzed aircraft CO_2 data over the Tokyo area and showed a strong influence of fossil-fuel CO_2 from East Asia (mainly China) in the free troposphere above 2 km over the surface. Therefore, it might be necessary to consider the contribution from the strong emissions in East Asia when estimating Tokyo emissions.

The National Institute for Environmental Studies (NIES) observes GHG concentrations continuously at a height of around 250 m at TOKYO SKYTREE (TST; 35.71°N, 139.81°E), a 634-m-high freestanding broadcasting tower. In this study, using the continuous TST observation data, we estimated net CO_2 fluxes from the megacity area of Tokyo for two years (2019 and 2020) in combination with a global high-resolution model simulation, which can consistently simulate flows from out of the target area (i.e., there is no boundary condition). To evaluate CO_2 fluxes from a local area, we performed a tagged tracer simulation, in which independent tracers from different sources were simulated in the model. We separated the atmospheric signals of the Tokyo local flux from those of other areas in the tagged tracer simulation, and the contributions from different sectors and regions were estimated quantitatively.

2. Data and Method

2.1 Observations

The atmospheric CO_2 concentrations at a height of approximately 250 m on TST have been measured by NIES with a cavity ring-down spectrometer analyzer (G2401, Picarro Inc.) since January 2017. CO_2 mole fractions were determined against three working standard gases that were calibrated against the NIES 09 CO_2 standard scale (Machida et al. 2011). In the target region, the nearly neutral mixing layer is maintained up to at least 250 m in summer season even at night. Even in winter, a strongly stable layer can form aloft, which may result in the mixed layer exceeding 200 m (Nakajima et al., 2018). Therefore, the observation height may be included within the mixed layer.

Considering the inhomogeneity of CO_2 fluxes is important to analyze variations of CO_2 concentrations because strong point sources are scattered around the observation point. Therefore, in addition to CO_2, we used ^{222}Rn (hereinafter simply called Rn) data in the analysis. Rn is a natural radioisotope with a half-life of 3.8 days and has a relatively homogeneous flux field over land. Because Rn is produced by decay of ^{226}Ra in soil, the land surface is the dominant global source, and the flux is often assumed to be constant over land (Jacob et al., 1997). To evaluate the effect of flux inhomogeneity, we performed a similar analysis for both Rn and CO_2. Rn concentrations are observed at the same height on TST as CO_2 concentrations with the electrostatic collection method developed by the National Institute of Advanced Industrial Science and Technology and the Meteorological Research Institute (MRI) of the Japan Meteorological Agency (Wada et al., 2010). Continuous observations of Rn started in February 2018.

2.2 Model simulation

We simulated atmospheric CO_2 concentrations at TST from January 2019 to December 2020 using the Nonhydrostatic ICosahedral Atmospheric Model (NICAM: Tomita and Satoh, 2004; Satoh et al., 2008, 2014). NICAM has been developed as a global high-resolution simulation (e.g., Kodama et al., 2021). The atmospheric tracer transport model version named NICAM-based Transport Model (NICAM-TM: Niwa et al., 2011) has been developed and used for CO_2 and other trace gas simulations by virtue of the perfect mass conservation property of NICAM. The NICAM original icosahedron consists of 20 triangles to describe the Earth, and this state is called as glevel-0. The "glevel-n" represents the grid division level. By dividing each triangle into four small triangles, n increases by 1 and the horizontal model resolution becomes higher. The shape of grid is hexagon, except that it is pentagon at only twelve points inherited from the original icosahedron's vertices. Because CO_2 is a long-lived tracer and requires a long-term simulation, NICAM-TM has been used with a low horizontal resolution of "glevel-5" or "glevel-6" (Niwa et al., 2012, 2021), corresponding to mean grid intervals of ~223 and 112 km, respectively. NICAM is a general circulation model, and wind velocities and directions modeled by NICAM were used for the wind analysis (Fig. S1).

We used NICAM-TM with the high resolution of glevel-9 (mean grid interval ~14 km) for the atmospheric CO_2 transport simulation (Fig. 1a). This horizontal resolution is the highest for our available computing resources to perform a two year-long integration. Ours is the first study to use the high-resolution NICAM for CO_2 simulation, though several studies of short-lived species or aerosols have already been performed (Ishijima et al., 2018; Goto et al. 2020). As demonstrated by Ishijima et al. (2018), synoptic variations are better simulated at a remote site by the high-resolution NICAM; however, that high-resolution model has not yet been used for assessing emissions at a local scale such as Tokyo. Usually, the glevel-9 of NICAM does not use a parameterization scheme for cumulus convection; however, we applied the cumulus convection scheme of the Chikira–Sugiyama Scheme (Chikira and Sugiyama, 2010) that has been used at lower resolutions for consistency with inverse analysis simulations. In contrast to the conventional studies with the high-resolution NICAM, we applied the nudging scheme with JRA-55 horizontal wind (Kobayashi et al., 2015) to reproduce real atmospheric transport fields, which is the usual approach with NICAM-TM. The numbers of the vertical layers are 40, and the center of the lowest layer is at ~81 m. That of the second layer is at ~249 m, which roughly corresponds to the observation altitude of TST, and that of the next layer is at 430m. A summary of the model setup is provided in Table 1.

The locations of TST, remote sites around Japan, and the Tokyo area that we define in this study are illustrated in Fig. 1. In this study, the Tokyo area is defined as the land within 50 km of the bay area of Tokyo (35.6°N, 139.8°E) to include point sources around Tokyo Bay. In this study, “CO_2tk” denotes the Tokyo-originated CO_2 concentration. "Tokyo" in this paper is different from Tokyo in terms of administrative divisions. This study focuses only on the Tokyo area, but we used the global model to reproduce CO_2 concentration variations. In fact, simulating atmospheric plumes in a scale comparable to or smaller than the horizontal model grid is challenging (Skamarock, 2004; Frehlich & Sharman, 2008; Sato et al., 2018). The global model was used to estimate CO_2 concentrations in a larger scale than the Tokyo area. Especially, the model calculated CO_2 concentrations originated from out of the Tokyo area, which this study defines as background concentrations (Sec. 2.5). Furthermore, in the analysis of CO_2 concentration variations at TST, we used wind speed thresholds to select well-mixed and highly representative data (Sec. 3.3).

To simulate atmospheric CO_2 concentrations comparable to observations from global to regional scales, we used inversion fluxes in which non-fossil-fuel fluxes were optimized by the NICAM-based Inverse Simulation for Monitoring CO_2 (NISMON-CO_2: Niwa, 2020; Niwa et al., 2022) with globally distributed observations. Atmospheric simulations in NISMON-CO_2 were performed by NICAM with glevel-5 (~223 km) resolution, and surface fluxes were optimized on 1° × 1° grids through a grid conversion scheme. The 1° × 1° inversion flux data thus produced were downscaled to the glevel-9 grids for the high-resolution simulation of this study. For the inverse analysis of NISMON-CO_2, fossil-fuel emissions were not optimized and other natural CO_2 fluxes were optimized. The Gridded Fossil Emissions Dataset (GridFED; Jones et al., 2021), which was produced by scaling data from the Emissions Database for Global Atmospheric Research (EDGAR; Janssens-

Maenhout et al., 2019), was used for the fixed fossil-fuel emissions in the inverse analysis. The same data, but regridded to the glevel-9 grid data of GridFED, were used in this study.

To evaluate the dependency of the fossil-fuel emissions dataset on the results of the analysis, we used additional fossil-fuel emissions data from the Open-source Data Inventory for Anthropogenic Carbon dioxide (ODIAC; Oda et al., 2018). The inventory is produced from information on emissions intensity and the locations of power plants and satellite-observed nighttime lights. The monthly mean fossil-fuel emissions of GridFED and ODIAC are both high around Tokyo Bay (Fig. 2a and b), but their distributions are slightly different on the east coast of Tokyo Bay (Fig. 2c). In contrast, on the western coast of Tokyo Bay, where strong emissions are present, the GridFED emissions are much larger than those of ODIAC. Furthermore, ODIAC emissions are slightly stronger in the northern part of the Tokyo area, where fossil-fuel emissions are relatively small. In the following analysis, unless otherwise noted, the GridFED but not ODIAC is used for the fossil fuel emissions.

In addition, Rn, which has fluxes over almost all land surfaces, was also simulated and compared with the observations. The Rn results were compared with those for CO_2 to evaluate the influence of the flux inhomogeneity. In the model, the flux distribution of Rn is set uniformly on the basis of latitude and whether the locality is land or ocean (Jacob et al., 1997). Fluxes from 60°N to 60°S on land and over the ocean are 1.0 and 0.005 atoms cm^{-2} s^{-1}, respectively; fluxes from 70°N to 60°N and 70°S to 60°S are 0.005 atoms cm^{-2} s^{-1}. The other fluxes around the poles are zero.

Observed one-hourly mean CO_2 concentrations display large variability, which cannot be correctly reproduced on brief timescales by the model. For a site such as TST, where strong emissions occur nearby, it is typically difficult to reproduce short-term concentration variations resulting from the large influence of small-scale turbulence. Because such model errors can be reduced by increasing the mean interval (Turnbull et al., 2016), we applied 12-h moving averages to both simulated and observed data.

2.3 Pre-comparison in remote sites

To test the model's basic performance in simulating variations of CO_2 concentrations, we used data from Hateruma Island (HAT; 24.06°N, 123.78°E; Mukai et al., 2014; Tohjima et al., 2020), in the Pacific Ocean southwest of the Japanese archipelago, and on Minamitorishima Island (MNM; 24.29°N, 153.98°E; Watanabe et al., 2000), the easternmost island belonging to Japan, where the influence of anthropogenic CO_2 emissions is very small (Fig. 1b). HAT, like TST, is operated by the NIES/the Center for Global Environment Research (CGER); MNM is operated by the Japan Meteorological Agency (JMA). Both HAT and MNM observed CO_2 concentrations with a nondispersive infrared absorption spectrometer analyzer during the target period. Comparisons of observed and calculated total CO_2 concentrations (CO_2tot) at HAT and MNM for 2019–2020 are illustrated in Fig. 3a and 3b, respectively. The correlation coefficients between the model simulation and the observation are 0.823 and 0.941 at HAT and MNM, respectively, with almost no bias. The good agreement between the model and the observations for both the remote sites suggests that the inversion flux from NISMON-CO_2 was successfully downscaled to the high-resolution NICAM (note that the observations at these two sites were used in the optimization of NISMON-CO_2; Niwa, 2020).

2.4 Tagged tracer

In this high-resolution simulation of NICAM-TM, several “tagged CO_2 tracers” were introduced. We separate flux data by source types and regions in the tagged tracer simulation. Atmospheric CO_2 concentrations from fossil-fuel emissions (CO_2ff), terrestrial biospheres (CO_2bio), and the ocean (CO_2ocn) were simulated separately. Moreover, atmospheric CO_2 concentrations from East Asia (China, North and South Korea, and Taiwan, but excluding Japan), Japan (including Tokyo), and Tokyo were also separately calculated; the Tokyo tracer was further separated into tracers from four zones and a TST-neighbor area to investigate local influences. The TST-neighbor consisted of the three NICAM grids closest to TST, and the area overlapped with the four Tokyo local zones (Fig. 1c). CO_2tot contains the atmospheric concentrations from all emissions (not only CO_2ff, CO_2bio, and CO_2ocn, but also other sources such as biomass burning) and all regions. Although the calculation in CO_2tot incorporates a sufficient spin-up period, calculation of the tagged tracers has no spin-up time. However, the flux distribution is located only near the observation point for tagged tracers, and the contribution of background variation caused by

Tokyo-originated flux relative to variations in CO_2 concentration is very small. Thus, the effect of the lack of spin-up time for tagged tracers can be ignored.

To quantify the contributions of CO_2 fluxes to variations of CO_2 concentrations at TST from different sectors and regions, we used the variance ratio (VR), which is calculated as the ratio of the CO_2 concentration variance of a tracer to that of another tracer over a 30 day-period; for example, to evaluate the impact of fossil fuel at TST, the VR was calculated from the ratio of the variance of CO_2ff to the variance of CO_2tot.

2.5 Estimation of Tokyo-originated CO_2

Background_CO_2 concentration for estimation of urban emissions could be determined only by observations, such as the value at upwind site or the daily minimum value. However, those methods may have limitation in tracking continuous changes or need to limit wind directions. Our study used the global model with the tagged tracers to calculate the background concentrations, which does not require any wind direction limitation and enables us to track continuous changes (Sec. 3.1). The background CO_2 concentration of the Tokyo area was derived from the NICAM simulation (CO_2bg^{NICAM}), which is defined as the simulated total CO_2 (CO_2tot^{NICAM}) minus the simulated Tokyo-originated CO_2 concentration (CO_2tk^{NICAM}):

$$CO_2bg^{NICAM} = CO_2tot^{NICAM} - CO_2tk^{NICAM}. \quad \text{(Eq. 1)}$$

CO_2tot^{NICAM} is calculated from all fluxes, while CO_2tk^{NICAM} considers only the fluxes from

Tokyo region in the calculation of the tagged tracer. Because the fluxes other than fossil-fuel emissions are derived from the inverse simulation, CO_2 concentrations should be globally well reproduced in the model. In fact, this assumption was confirmed by the good agreement of CO_2tot between the model and the observations at the remote sites, where influences from fossil-fuel emissions are small (Section 2.3). Therefore, it is reasonable to also use CO_2bg^{NICAM} for the background value of the observations. Thus, the Tokyo-originated CO_2 concentrations of the observations (CO_2tk^{Obs}) can be estimated by subtracting CO_2bg^{NICAM} from observed total CO_2 (CO_2tot^{Obs}):

$$CO_2tk^{Obs} = CO_2tot^{Obs} - CO_2bg^{NICAM}. \qquad \text{(Eq. 2)}$$

In this study, we compared CO_2tk^{Obs} and $CO2tk^{NICAM}$ using a standardized major axis linear regression, the slope of which is used to evaluate emissions. The slope of the linear regression is much less sensitive to outlier values than the ratio of the mean value or median value (Turnbull et al., 2015; Miller et al., 2012). Since both CO_2tk^{Obs} and $CO2tk^{NICAM}$ were defined using the same background concentration, the linear regression was calculated with the intercept fixed to zero.

3. Results

3.1 Comparison between the model simulation and the observations

The monthly VRs of CO_2 concentrations at TST are illustrated in Fig. 4. The VRs of CO_2ff of both GridFED and ODIAC were large, and their magnitudes were greater than 0.6

for all months (Fig. 4a). The VR of CO_2bio increased from late spring to autumn, but it was much smaller than CO_2ff. The VR of CO_2ocn was negligible. The VR of CO_2ff was large in winter, with small maxima also occurring in July. Suppression of vertical mixing and increased fossil-fuel consumption might have caused the winter increment of CO_2ff in urban areas (Moriwaki and Kanda, 2004; Xueref-Remy et al., 2018).

The VR of CO_2 concentrations from each region from which a tagged tracer was simulated are shown in Fig. 4b. For CO_2ff, the annual mean VR of East Asia relative to all regions was less than 0.03 at TST. In contrast, the value for the Tokyo area was 0.87; thus, CO_2 emissions from the Tokyo area were dominant at TST. If the effect from areas outside of Japan is strong near the surface, the boundary condition becomes important when a regional model is used. Our study used a global model, which did not require boundary conditions. In fact, previous studies have suggested that effects from East Asia on Japan are large in terms of synoptic-scale variation (Tohjima et al., 2010) and that the influence of CO_2 from East Asia cannot be ignored in the free troposphere over Tokyo (Shirai et al. 2012). However, our results showed that the influence of areas outside Japan, such as China, was very weak at TST in terms of short-term (daily-scale) variation.

When CO_2ff from the Tokyo area was divided into the contributions from the four zones, VR of CO_2ff from ZSW (the southwest zone of the Tokyo area) to the whole Tokyo area was 0.4–0.9 and dominant. During summer, particularly strong VR was simulated from ZSW (Fig. 4c), where strong emissions from power plants and industrial areas occur south of TST along Tokyo Bay (Fig. 2a).

The time-series of CO_2tot at TST are illustrated in Fig. 5a. CO_2tot in NICAM basically reproduced the observations; however, the simulated values were sometimes larger than the observations. Nevertheless, the frequency of large overestimations was small: fewer than 3% of data were overestimated by more than 10%. Figure 5b shows the simulated and observed time-series of CO_2tk at TST. The fact that the variation of the difference of CO_2tk between the model and the observation was almost the same as that of the CO_2tot difference demonstrated the dominant contribution from the Tokyo area, as already indicated by the VR results (Fig. 4b).

Around Tokyo Bay, the predominant wind directions are north and south (Fig. 5d) because of the sea breeze (Yamato et al., 2017). The northern winds are further divided into northwesterly winds blowing from inland and northeasterly winds blowing from the Pacific side. Therefore, we defined three wind directions as follows: NE (azimuth degree 0–120° clockwise from north; 30% of all period); S (120–270°; 41%); and NW (270–360°; 29%). S-wind is the most frequent wind during summer because of the development of sea breezes at that time of year under the weak pressure gradient associated with the Pacific anticyclone (Yamato et al., 2017). In fact, southerly winds caused by the sea breeze transport an airmass with large CO_2ff. The frequency of S-wind carrying large CO_2ff is high in summer and causes the large VR of CO_2ff in July (Fig. 4a). In particular, from late July to early August of 2019, the observed CO_2tk was higher than that in other months by approximately 20–30 ppm (Fig.

5b). This marked increase is well reproduced in the model calculation. During this period, the wind direction was continuously from the south (Fig. 5d). The continuous southerly wind carried air parcels from sources around Tokyo Bay and caused the large CO_2tk at TST. If the background concentration was estimated only by using observational data, it would be difficult to capture such changes. The CO_2 background concentration estimation method using the observed daily minimum value would not be able to capture those continuous changes. In background estimation using multiple tower observations, available data is limited by the tower locations and wind direction because it is important to select sampling locations corresponding to the upwind and downwind positions of the emission source. This continuous elevation of CO_2 concentrations can be appropriately recognized as being derived from the Tokyo area thanks to the tagged tracer in the model.

3.2 Wind effect on CO_2

As demonstrated in Fig. 2, fossil-fuel emissions in Tokyo are stronger in the southern region, around Tokyo Bay, where many industrial areas and power plants are located. This flux inhomogeneity induces remarkable variations of CO_2tk with changes of wind speed and direction. Figs. 6a and 7a show the two-dimensional histogram in log-scale of the observed CO_2tk versus wind speed and direction, respectively. The frequency of high observed CO_2tk values gradually decreases with increasing wind speed; however, it is possible, although infrequent, to observe large CO_2tk even at wind speeds higher than 10 m s^{-1} (Fig. 6a).

Because of the existence of high emissions around Tokyo Bay, S-wind causes the observed CO_2tk values to be larger than the values associated with other wind directions (Fig. 7a). The difference between calculated and observed CO_2tk (ΔCO_2tk) depends on wind velocity: for low wind speeds, the model frequently simulated CO_2tk values larger than the observations (Fig. 6b). ΔCO_2tk also depended on wind direction: under S-wind conditions, when the observed CO_2tk was large, ΔCO_2tk was also large in comparison with the values for other directions (Fig. 7d).

The ΔCO_2tk data were divided at the median wind speed of 5.5 m s^{-1} into the upper 50% and lower 50% of cases. In May to June and August to September, low wind speeds dominated (53%–67%), but in other months, the frequency of high wind speeds was greater (>52%). Under high-wind-speed conditions, the model generally reproduced observations of CO_2tk (Fig. 7c, f). However, under low-wind-speed conditions, the model tended to overestimate CO_2tk frequency (Fig. 7b). In particular, during southern winds, ΔCO_2 of around 10 ppm was the most frequently observed value (Fig. 7e).

The VR of CO_2ff from the Tokyo area and the four Tokyo zones relative to total CO_2ff calculated with respect to wind speed are illustrated in Fig. 8. The VR of the Tokyo area decreased slightly with increasing wind speed, but the amount of decrease was very small. The VR for areas outside of Tokyo was almost zero. In addition, the VR of TST-neighbor did not show a clear change in response to wind speed. Even under high wind speeds, the VR of TST-neighbor did not reach zero, thus the influence of TST-neighbor on TST persisted.

Changes of the VR of the other zones were small. To summarize, the impact of each region varied slightly with wind speed, but the changes were not notably large, even under high-wind conditions (wind speeds ≥ 10 m s^{-1}); thus, even in strong winds, the impact of emissions from the Tokyo area remained important.

3.3 Effects of wind speed limitation

The seasonal changes of the slopes of the linear regression and the correlation coefficients of CO_2tk between the model simulation and the observation (means of the data shown in Fig. S2) for all, high (>5.5 m s^{-1}), and low (<5.5 m s^{-1}) wind speed conditions are illustrated in Fig. 9. Under all wind conditions, the slope of the regression line showed marked variations of approximately 1.2 to 1.8 (Fig. 9a). The slope of the regression line approached 1 and the correlation coefficient increased in spring and autumn, albeit at slightly different times. Because CO_2 emissions from GridFED for the Tokyo area were also relatively low in spring and autumn, these seasonal variations of the regression slope and correlation coefficient may be attributed to the seasonal changes in GridFED (Fig. S3).

The slope of the regression line was markedly different for different wind speeds: for high wind speeds, the slope was stable at approximately 1 throughout the year (Fig. 9a). However, the correlation coefficient did not show a clear trend between low and high wind speeds. Overall, high wind speeds tended to have a higher correlation coefficient, but there were cases in which low wind speeds had a higher coefficient (Fig. 9b).

To examine the effect of wind speeds, we performed a regression analysis with the modeled and observed CO_2tk values and changed the wind-speed threshold below which data were removed (Fig. 10a and b). The slope of the linear regression between observed and modeled CO_2tk became small when the low wind speeds were removed (Fig. 10a). In particular, the slope constantly decreased under low-wind-speed conditions, whereas the correlation coefficient increased with lower wind speeds (Fig. 10b). The correlation coefficient was greatest when results for wind speeds below 5.5 m s^{-1} were removed. Increasing the data-removal threshold resulted in the slope's becoming almost fixed. Over a wind-speed threshold of 7.0 m s^{-1}, the slope remained nearly constant at 0.93.

The slopes of regression lines and correlation coefficients of CO_2tk between the observation and the model for the three wind directions are illustrated in Fig. 10c and d. The number of S-wind data was greater than the number of either the NE- or NW-wind data: the proportions of data under S-, NE-, and NW-wind were 41%, 30%, and 29%, respectively, for all wind speeds, and 38%, 24%, and 37%, respectively, for high wind speeds. The alterations in slope for each wind direction were similar to that of all wind directions, i.e., removing low wind speeds reduced the slope (Fig. 10c). Especially under a S-wind, the slope became almost fixed and approximately 1 by removing low-wind-speed data. Thus, the simulation under S-wind conditions reproduced observations that were affected by the smoothed southern region by removing low-wind-speed data. However, the standard deviations under NE- and NW-wind conditions were larger than those under S-wind conditions. For a NE- or

NW-wind, the slopes did not become stable, even if low-wind-speed data were removed, and the reliability was low. In contrast, the correlation coefficients exhibited marked differences with different wind directions (Fig. 10d). Correlation coefficients under NW- and NE-wind conditions gradually decreased with fluctuations; however, the S-wind correlation coefficient increased with rising wind threshold, even for low wind speeds, the same pattern as for the all-wind-direction data.

3.4 Comparison of fossil-fuel emissions between GridFED and ODIAC

We mainly used GridFED for fossil-fuel emissions for the model simulation; however, we also considered the ODIAC results, for comparison. A comparison of the flux distribution between GridFED and ODIAC revealed that the GridFED emissions were much stronger than those from ODIAC on the west coast of Tokyo Bay, but those from ODIAC were slightly larger in the northern part of the Tokyo area (Fig. 2c). The larger emissions in GridFED made a larger contribution to CO_2ff than those of ODIAC during the summer months, when the S-wind blew frequently; however, the VR of ODIAC was slightly larger from January to March, when the northern winds were dominant (Fig. 4a).

Both the slope of the linear regression and the correlation coefficient between the observed and modeled CO_2tk were smaller for ODIAC than for GridFED, but the dependency on wind speed was almost the same for both simulation cases (Fig. 10a and b). The correlation coefficient between the model and the observations was greatest at a threshold of 5.0 or 5.5 m s^{-1}.

For ODIAC, the dependencies on wind-speed threshold were similar to those of GridFED for all wind directions (Fig. 10e and f). However, the magnitude of the S-wind regression-line slope of ODIAC was particularly small, and the slopes for the other wind directions were slightly larger than those of GridFED. The small slope was caused by the weaker emissions of ODIAC than GridFED on the west coast of Tokyo Bay. In contrast, the fact that the slopes of ODIAC under NE- and NW-wind conditions were slightly larger than those of GridFED was the result of the slightly larger ODIAC emissions in the northern zones of the Tokyo area (Fig. 2c).

3.5 Comparison of wind dependency between CO_2 and Rn

Although the reproducibility of the model was not necessarily determined drastically by its horizontal resolution (Nassar et al., 2013), it is possible that the increasing correlation coefficient and decreasing slope in Fig. 10 were caused by inadequate representation of atmospheric transport or surface fluxes in the model. In particular, the latter possibility is plausible because the CO_2 flux distribution in Tokyo is quite inhomogeneous. Although there were differences in the flux distribution between GridFED and ODIAC, they were basically similar, with strong fluxes at point sources around Tokyo Bay and weaker fluxes in other areas. This similarity probably led to the result that the dependencies of the regression-line slopes and correlation coefficients between the model and the observations were similar to each other for the wind data. To investigate whether the changes in the regression slopes and correlation coefficients resulted from insufficient model transport performance or from the inhomogeneity of the CO_2 flux distribution, we analyzed Rn, which has a flux distribution that differs from that of CO_2, and compared it with the CO_2 case using the same method as before.

In the time-series of Rn concentrations, simulated Rn was sometimes larger than the observed concentration (Fig. 5c), similarly to the simulated CO_2 concentrations; however, the timing of large differences between calculations and observations for Rn differed from that for CO_2. It is possible that the flux of Rn was overestimated in the model.

The seasonal variations in the slope of the linear regression and correlation coefficient of Rn between the model and the observation (monthly means of the data shown in Fig. S4) are illustrated in Fig. 11. The regression-line slope of Rn showed a more distinct seasonal pattern compared to CO_2, and it increased notably from spring to summer. The difference between the high and low wind speeds, separated using the threshold of 5.5 m s^{-1}, was particularly large during this period, and a marked contrast observed, especially in June and July. The correlation coefficient of Rn was larger than that of CO_2 because the flux distribution of Rn was simpler than that of CO_2. Changes in the correlation coefficient, unlike those of CO_2, show less clear seasonal variations. Similar to CO_2, data for high wind speeds tended to have a higher correlation coefficient in general. Furthermore, the timing of changes in the regression-line slope and the correlation coefficient did not necessarily align with each other.

The slope of the regression line also decreased with increasing wind-speed threshold (Fig. 10c), similar to CO_2tk, but the slope was greater than 1, even for a threshold wind speed of 10 m s^{-1}. The correlation coefficient of Rn generally increased with increasing wind speed (Fig. 10d), in contrast to CO_2, which rose only under low-wind-speed conditions. If the insufficient model transport performance were the only cause of the large overestimation of CO_2tk and the relationship between CO_2tk and wind speed, the relationship between Rn and wind speed should be the same as that between CO_2tk and wind speed. However, the decrease in the regression-line slope and the rise in the correlation coefficient of Rn was stronger than the patterns of CO_2tk for all wind directions.

In the same way as CO_2, the regression-line slope and correlation coefficient of Rn concentration were considered separately for each wind direction (Fig. 10c and d). Under NW-wind conditions, increasing the wind speed threshold resulted in a decrease of the slope and an increase of the correlation coefficient. Under S-wind, the slope decreased, but by a smaller amount than for NW winds; in addition, the increase in correlation coefficient for S-wind was gradual. The NE-wind showed a more obvious decrease in slope than the other two wind directions. In addition, for the NE-wind, the correlation coefficient decreased with rising wind-speed threshold, but with some variability. Unlike CO_2tk, under S-wind conditions, the correlation coefficient of Rn did not increase under low-wind-speed conditions. The regression slopes under S- and NW-wind conditions slowly fell, even under high-wind-speed conditions, but they remained greater than 1. Thus, the Rn concentration in the model was overestimated, even if the flux distribution was smoothed by removing low-wind-speed data, as a result of overestimation of the fluxes provided to the model. One reason for the overestimation may have been the covering of the surface with asphalt and thus prevention of an Rn flux in the urban area, but it is also possible that the Rn flux input to the model was too high. In contrast, the slope of CO_2tk under high wind speeds and S-wind conditions was stable at approximately 1, and the model under high-wind-speed conditions reproduced the observations. The comparison with Rn revealed that the changes of regression on CO_2tk were mostly caused by flux inhomogeneity, but the insufficient flux inhomogeneity could be smoothed by removing low-wind-speed data. This tendency was more pronounced under S-wind conditions, which were strongly influenced by the coastal region with abundant emissions.

3.6 Estimation of net CO_2 flux from Tokyo

To estimate the net CO_2 flux from Tokyo, we obtained an optimal slope to represent the Tokyo area of 0.93 ± 0.08 by removing data with a threshold wind speed larger than 7 m s^{-1}. We selected this wind-speed because the slope became constant above this threshold. The annual mean CO_2 fluxes in Tokyo area, within the circle of 50km radius, of GridFED for fossil fuel and VISIT for the biosphere were 9.4 and −0.1 kg C m^{-2} $year^{-1}$, respectively. From this prior estimate of 9.3 kg C m^{-2} $year^{-1}$, which is the sum of the fossil fuel emission and the biosphere flux, the net CO_2 flux from Tokyo (which contains both land and ocean areas) was corrected by dividing the optimal slope, yielding a value of 10.1 ± 0.8 kg C m^{-2} $year^{-1}$. Multiplying the corrected flux value with the defined area, we obtained a value of 79.5 ± 6.6 Tg C $year^{-1}$ for integrated net emissions from the Tokyo area. This flux included both land and ocean components, and so the magnitude was smaller than that of the land-only flux.

For ODIAC, when the same method as that for GridFED was applied, the optimal CO_2tk slope was 0.74 ± 0.07. The mean annual net CO_2 flux in the Tokyo area was 6.8 kg C m^{-2} $year^{-1}$ with ODIAC; thus, the net CO_2 flux from Tokyo corrected by the optimal slope was 9.1 ± 0.9 kg C m^{-2} $year^{-1}$ (71.8 ± 6.8 Tg C $year^{-1}$), which was smaller by approximately 10% than the value obtained with GridFED.

4. Discussion and Conclusion

4.1 Insufficient representativeness of TST

We applied TST to analyze emissions from the Tokyo area; however, the results indicated that CO_2 concentration variations at TST were mainly affected by ZSW and not as much by ZSE. Therefore, only using TST was not sufficient to investigate the influence of the whole Tokyo area. Although the intensity of the flux on the east coast of Tokyo Bay was approximately 70% of that of the west coast, the VR of ZSE (which includes the east coast emissions) was lower than 0.1 and much smaller than the VR of ZSW (Fig. 8). This difference was attributable to the less frequent easterly winds toward TST (Fig. 5d and Fig. S1). Thus, further observations that can capture signals from the east coast of Tokyo Bay are needed to evaluate the entirety of Tokyo emissions more accurately.

4.2 Comparison with previous studies and original bottom-up modeling

In the simulation of CO_2 using GridFED, although estimated CO_2tk was sometimes overestimated, the overestimations were excluded under high-wind-speed conditions. Removing low-wind-speed data induced an increment of the correlation coefficient between simulation and observation, and the regression slope became stable. In contrast, the regression slope of Rn continued to decrease under high-wind-speed conditions and did not become stable. Thus, whether the regression slope became stable by excluding low wind speeds depended on the flux distribution, and one of the causes of the CO_2tk overestimation may have been the flux distribution in GridFED. Similar results were obtained with ODIAC. By excluding the low-wind-speed data, the influence of flux inhomogeneity was smoothed, and a stable regression line could be estimated for all seasons. Although removing low-wind-speed data changed the impact from the TST vicinity, this removal did not always eliminate local influences (Fig. 8). We estimated the net CO_2 flux from Tokyo to be 10.1 ± 0.8 kg C m^{-2} $year^{-1}$ (79.5 ± 6.6 Tg C $year^{-1}$) with GridFED, calculated by using the optimal slope of the regression line.

The estimation obtained by using GridFED was consistent with those of previous studies in an approximately similar target area: emissions of 75.8 Tg C $year^{-1}$ (Ohyama et al., 2023) were calculated by an inversion analysis based on observations of ground-based Fourier transform spectrometers around Tokyo, and a value of 70 ± 21 ± 6 Tg C $year^{-1}$ (Babenhauserheide et al., 2020) was derived from a combination of Fourier transform infrared and radiosonde meteorological observations around Tokyo. Comparing the flux estimates for the Tokyo area obtained in the present and previous studies showed that our result from GridFED was approximately 9% larger than that obtained with the original GridFED (Fig. 12). Our value was also larger than those obtained in previous studies, but the differences could not be discussed in detail because the target regions were not exactly the same. The difference between our estimate obtained with ODIAC and the original estimate was more notable—our estimate was approximately 1.4 times the original. This difference was consistent with the fact that the two previous studies (Babenhauserheide et al., 2020; Ohyama et al., 2023) have noted that their estimations were larger than those obtained by using ODIAC. Therefore, it is likely that Tokyo-originated emissions inferred by using bottom-up methods, especially ODIAC, were underestimated.

To summarize, we successfully estimated the net CO_2 flux from Tokyo, one of the largest cities in the world, using observations at TST and the high-resolution NICAM with tagged tracers. For future study, additional observation points on the east coast of Tokyo Bay will be necessary to improve the estimate of emissions from the whole Tokyo area. By performing a higher resolution calculation with a regional model and focusing on the urban area, the reproducibility of CO_2 concentrations within the Tokyo area and the flux estimation could be further improved.

Data Availability Statement

NICAM and NICAM-TM can be obtained by applying through the inquiry form on [https://nicam.jp/dokuwiki/doku.php].

The flux data of NISMON-CO_2, GridFED, and ODIAC are available at [https://doi.org/10.17595/20201127.001], [https://doi.org/10.5281/zenodo.4277266], and [https://doi.org/10.17595/20170411.001], respectively.

The data of CO_2 and Rn observed at TST supporting the findings of this study are available from NIES and MRI, respectively. Restrictions apply to the availability of these data, which were used under license for the current study and are not publicly available. The data are available from the authors upon reasonable request, subject to permission from NIES and MRI, respectively.

The data for CO_2 observed at HAT are available from Mukai et al. (2014). The data for CO_2 observed at MNM were obtained from the World Data Centre for Greenhouse Gases (https://gaw.kishou.go.jp).

Acknowledgments

This research was performed by the Environment Research and Technology Development Fund (JPMEERF21S20810) of the Environmental Restoration and Conservation Agency provided by the Ministry of the Environment of Japan. We thank Toshinobu Machida and Motoki Sasakawa at NIES for their support to prepare the standard gases used in this study. The simulations were completed with the NEC SX-Aurora TSUBASA supercomputer at NIES. Wind data observed at TST around 250m height were provided by TOBU TOWER SKYTREE Co., Ltd. Constructive comments from two anonymous reviewers helped improve our manuscript.

References

Arioli, M. S., M. d. A. D'Agosto, F. G. Amaral, & H. B. B. Cybis, H. B. B., 2020: The evolution of city-scale GHG emissions inventory methods: A systematic review. *Environ. Impact Assess. Rev.*, **80**, 106316.

Babenhauserheide, A., F. Hase, & I. Morino, 2020: Net CO_2 fossil fuel emissions of Tokyo estimated directly from measurements of the Tsukuba TCCON site and radiosondes. *Atmos. Meas. Tech.*, **13(5)**, 2697-2710.

Chikira, M., & M. Sugiyama, 2010: A cumulus parameterization with state-dependent entrainment rate. Part I: Description and sensitivity to temperature and humidity profiles. *J. Atmos. Sci.*, **67(7)**, 2171-2193.

Frehlich, R., & R. Sharman, 2008: The use of structure functions and spectra from numerical model output to determine effective model resolution. *Mon. Weather Rev.*, **136(4)**, 1537-1553.

Goto, D., Y, Sato, H. Yashiro, K. Suzuki, E. Oikawa, R. Kudo, ... & T. Nakajima, 2020: Global aerosol simulations using NICAM. 16 on a 14 km grid spacing for a climate study: Improved and remaining issues relative to a lower-resolution model. *Geosci. Model Dev.*, **13(8)**, 3731-3768.

Hirano, T., H. Sugawara, S. Murayama, & H. Kondo, 2015: Diurnal variation of CO_2 flux in an urban area of Tokyo. *Sola*, **11**, 100-103.

Iida, Y., Y. Takatani, A. Kojima, & M. Ishii, 2021: Global trends of ocean CO_2 sink and ocean acidification: an observation-based reconstruction of surface ocean inorganic carbon variables. *J. Oceanogr.*, **77(2)**, 323-358.

IPCC, 2022: Summary for Policymakers. In: Climate Change 2022: Impacts, Adaptation, and Vulnerability. Contribution of Working Group II to the Sixth Assessment Report of the Intergovernmental Panel on Climate Change. Cambridge University Press, Cambridge, UK and New York, NY, USA, pp. 3-33, doi:10.1017/9781009325844.001.

Ishijima, K., M. Takigawa, Y. Yamashita, H. Yashiro, C. Kodama, M. Satoh, ... & S. Hirao, 2018: Analysis of high radon-222 concentration events using multi-horizontal-resolution NICAM simulations. *SOLA*, **14**, 111-115.

Ito, A., 2019: Disequilibrium of terrestrial ecosystem CO_2 budget caused by disturbance-induced emissions and non-CO2 carbon export flows: a global model assessment, *Earth*

Syst. Dynam., **10**, 685–709, https://doi.org/10.5194/esd-10-685-2019, 2019.

Jacob, D. J., M. J. Prather, P. J. Rasch, R. L. Shia, Y. J. Balkanski, S. R. Beagley, ... & P. Zimmermann, 1997: Evaluation and intercomparison of global atmospheric transport models using 222Rn and other short-lived tracers. *J. Geophys. Res.: Atmos.*, **102(D5)**, 5953-5970.

Janssens-Maenhout, G., M. Crippa, D. Guizzardi, M. Muntean, E. Schaaf, F. Dentener, ... & G. D. Oreggioni, 2019: EDGAR v4. 3.2 Global Atlas of the three major greenhouse gas emissions for the period 1970–2012. *Earth Syst. Sci. Data*, **11(3)**, 959-1002.

Jones, M. W., R. M. Andrew, G. P. Peters, G. Janssens-Maenhout, A. J. De-Gol, P. Ciais, ... & C. Le Quéré, 2021: Gridded fossil CO_2 emissions and related O_2 combustion consistent with national inventories 1959–2018. *Sci. Data*, **8(1)**, 2.

Kobayashi, S., Y. Ota, H. Harada, A. Ebita, M. Moriya, H. Onoda, K. Onogi, H. Kamahori, C. Kobayashi, H. Endo, K. Miyaoka, & K. Takahashi, 2015: The JRA-55 Reanalysis: General Specifications and Basic Characteristics, *J. Met. Soc. Japan*, **93**, 5-48, doi: 10.2151/jmsj.2015-001.

Kodama, C., T. Ohno, T. Seiki, H. Yashiro, A. T. Noda, M. Nakano, ... & M, Sugi, 2021: The Nonhydrostatic ICosahedral Atmospheric Model for CMIP6 HighResMIP simulations (NICAM16-S): Experimental design, model description, and impacts of model updates. *Geosci. Model Dev.*, **14(2)**, 795-820.

Lauvaux, T., N. L. Miles, A. Deng, S. J. Richardson, M. O. Cambaliza, K. J. Davis, ... & K.

Wu, 2016: High-resolution atmospheric inversion of urban CO_2 emissions during the dormant season of the Indianapolis Flux Experiment (INFLUX). *J. Geophys. Res.: Atmos.*, **121(10)**, 5213-5236.

Long, Y., & Y. Yoshida, 2018: Quantifying city-scale emission responsibility based on input-output analysis–Insight from Tokyo, Japan. *Appl. Energy*, **218**, 349-360.

Machida, T., Y. Tohjima, K. Katsumata, & H. Mukai, 2011: A new CO_2 calibration scale based on gravimetric one-step dilution cylinders in National Institute for Environmental Studies-NIES09 CO_2 scale. Paper presented at: Report of the 15th WMO Meeting of Experts on Carbon Dioxide Concentration and Related Tracer Measurement Techniques; September2009; Jena, Germany, WMO/GAW Rep. 194, edited by: Brand, W., 165–169, WMO, Geneva, Switzerland.

Miles, N. L., K. J. Davis, S. J. Richardson, T. Lauvaux, D. K. Martins, A. J. Deng, ... & J. C. Turnbull, 2021: The influence of near-field fluxes on seasonal carbon dioxide enhancements: results from the Indianapolis Flux Experiment (INFLUX). *Carbon Balance Manag.*, **16**, 1-15.

Miller, J. B., S. J. Lehman, S. A. Montzka, C. Sweeney, B. R. Miller, A. Karion, ... & P. P. Tans, 2012: Linking emissions of fossil fuel CO_2 and other anthropogenic trace gases using atmospheric $^{14}CO_2$. *J. Geophys. Res. Atmos.*, **117(D8)**.

Moriwaki, R., & M. Kanda, 2004: Seasonal and diurnal fluxes of radiation, heat, water vapor, and carbon dioxide over a suburban area. *J. Appl. Meteorol. Climatol.*, **43(11)**, 1700-1710.

Mukai et al., 2014: Continuous observational data of atmospheric CO_2 mixing ratios on Hateruma Island, Ver.1.5, Center for Global Environmental Research, National Institute for Environmental Studies, DOI:10.17595/20160901.001. (Reference date: 2024/01/01)

Nakajima, K., H. Takahasji, H. Yokoyama, & N. Tsunematsu, 2018: Vertical Structures of Nocturnal Potential Temperature under Clear and Weak Wind Conditions in the Central Urban Area of Tokyo, Japan: Statistical Analysis Using Observation Data at Tokyo Tower, *Geographical Review of Japan Series A*, **91-1**, 24-42, https://doi.org/10.4157/grj.91.24 (in Japanese).

Nakanishi, M. & H. Niino, 2004: An improved Mellor–Yamada level-3 model with condensation physics: Its design and verification. *Bound.-Layer Meteorol.*, **112(1)**, 1-31.

Nassar, R., L. Napier-Linton, K. R. Gurney, R. J. Andres, T. Oda, F. R. Vogel, & F. Deng, 2013: Improving the temporal and spatial distribution of CO_2 emissions from global fossil fuel emission data sets. *J. Geophys. Res. Atmos.*, **118(2)**, 917-933.

Niwa, Y., H. Tomita, M. Satoh, & R. Imasu, 2011: A three-dimensional icosahedral grid advection scheme preserving monotonicity and consistency with continuity for atmospheric tracer transport. *J. Meteorol. Soc. Japan. Ser. II,* **89(3)**, 255-268.

Niwa, Y., T. Machida, Y. Sawa, H. Matsueda, T. J. Schuck, C. A. Brenninkmeijer, ... & M. Satoh, 2012: Imposing strong constraints on tropical terrestrial CO_2 fluxes using passenger aircraft based measurements. *J. Geophys. Res. Atmos.*, **117(D11)**.

Niwa, Y., 2020: Long-term global CO_2 fluxes estimated by NICAM-based Inverse Simulation for Monitoring CO_2 (NISMON-CO_2). https://doi.org/10.17595/20201127.001.

Niwa, Y., Y. Sawa, H. Nara, T. Machida, H. Matsueda, T. Umezawa, ... & Y. Tohjima, 2021: Estimation of fire-induced carbon emissions from Equatorial Asia in 2015 using in situ aircraft and ship observations. *Atmos. Chem. Phys.*, **21(12)**, 9455-9473.

Niwa, Y., K. Ishijima, A. Ito, & Y. Iida, 2022: Toward a long-term atmospheric CO_2 inversion for elucidating natural carbon fluxes: technical notes of NISMON-CO2 v2021. 1. *Prog. Earth Planet. Sci.*, **9(1)**, 1-19.

Noda, A. T., K. Oouchi, M. Satoh, H. Tomita, S. Iga, & Y. Tsushima, 2010: Importance of the subgrid-scale turbulent moist process: Cloud distribution in global cloud-resolving simulations. *Atmos. Res.*, **96(2-3)**, 208-217.

Oda, T., S. Maksyutov, & R. J. Andres, 2018: The Open-source Data Inventory for Anthropogenic CO_2, version 2016 (ODIAC2016): a global monthly fossil fuel CO_2 gridded emissions data product for tracer transport simulations and surface flux inversions, *Earth Syst. Sci. Data*, doi:10.5194/essd-10-87-2018.

Ohyama, H., M. M. Frey, I. Morino, K. Shiomi, M. Nishihashi, T. Miyauchi, ... & F. Hase, 2023: Anthropogenic CO_2 emission estimates in the Tokyo Metropolitan Area from ground-based CO_2 column observations. *EGUsphere*, **2023**, 1-38.

Sato, Y., M. Takigawa, T. T. Sekiyama, M. Kajino, H. Terada, H. Nagai, ... & T. Nakajima, 2018: Model intercomparison of atmospheric 137Cs from the Fukushima Daiichi Nuclear Power Plant accident: Simulations based on identical input data. *J. Geophys. Res.*,

123(20), 11-748.

Satoh, M., T. Matsuno, H. Tomita, H. Miura, T. Nasuno, & S. I. Iga, 2008: Nonhydrostatic icosahedral atmospheric model (NICAM) for global cloud resolving simulations., *J. Comput. Phys.*, **227(7)**, 3486-3514.

Satoh, M., H. Tomita, H. Yashiro, H. Miura, C. Kodama, T. Seiki, ... & H, Kubokawa, 2014: The non-hydrostatic icosahedral atmospheric model: Description and development. *Prog. Earth Planet. Sci.*, **1(1)**, 1-32.

Shirai, T., T. MacHida, H. Matsueda, Y. Sawa, Y. Niwa, S. Maksyutov, & K. Higuchi, 2012: Relative contribution of transport/surface flux to the seasonal vertical synoptic CO_2 variability in the troposphere over Narita. *Tellus B Chem. Phys. Meteorol.*, **64(1)**, 19138.

Skamarock, W. C., 2004: Evaluating mesoscale NWP models using kinetic energy spectra. *Mon. Weather Rev.*, **132(12)**, 3019-3032.

Sun, L., W. Liu, Z. Li, B. Cai, M. Fujii, X. Luo, ... & Y. Le, 2021: Spatial and structural characteristics of CO_2 emissions in East Asian megacities and its indication for low-carbon city development. *Appl. Energy*, **284**, 116400.

Tohjima, Y., H. Mukai, S. Hashimoto, & P. K. Patra, 2010: Increasing synoptic scale variability in atmospheric CO_2 at Hateruma Island associated with increasing East-Asian emissions. *Atmos. Chem. Phys.*, **10(2)**, 453-462.

Tohjima, Y., P. K. Patra, Y. Niwa, H. Mukai, M. Sasakawa, & T. Machida, 2020: Detection of fossil-fuel CO_2 plummet in China due to COVID-19 by observation at Hateruma. *Sci.*

Rep., **10(1)**, 18688.

Tomita, H. & M. Satoh, 2004: A new dynamical framework of nonhydrostatic global model using the icosahedral grid. *Fluid Dyn. Res.*, **34(6)**, 357.

Turnbull, J. C., C. Sweeney, A. Karion, T. Newberger, S. J. Lehman, P. P. Tans, ... & I. Razlivanov, 2015: Toward quantification and source sector identification of fossil fuel CO_2 emissions from an urban area: Results from the INFLUX experiment. *J. Geophys. Res. Atmos.*, **120(1)**, 292-312.

Turnbull, J. C., E. D. Keller, M. W. Norris, & R. M. Wiltshire, 2016: Independent evaluation of point source fossil fuel CO_2 emissions to better than 10%. *Proc. Natl. Acad. Sci.*, **113(37)**, 10287-10291.

UN. Population Division, 2018: The World's cities in 2018: data booklet, The 2018 Revision Rep., United Nations.

Van Der Werf, G. R., J. T. Randerson, L. Giglio, T. T. Van Leeuwen, Y. Chen, B. M. Rogers, ... & P. S. Kasibhatla, 2017: Global fire emissions estimates during 1997–2016. *Earth Syst. Sci. Data*, **9(2)**, 697-720.

Wada, A., S. Murayama, H. Kondo, H. Matsueda, Y. Sawa, & K. Tsuboi, 2010: Development of a compact and sensitive electrostatic radon-222 measuring system for use in atmospheric observation. *J. Meteorol. Soc. Japan*, **88(2)**, 123-134.

Watanabe, F., O. Uchino, Y. Joo, M. Aono, K. Higashijima, Y. Hirano, ... & K. Suda, 2000: Interannual Variation of Growth Rate of Atmospheric Carbon Dioxide Concentration

Observed at the JMA's Three Monitoring Stations Large Increase in Concentration of Atmospheric Carbon Dioxide in 1998. *J. Meteorol. Soc. Japan Ser. II,* **78(5)**, 673-682.

World Bank, 2010: Cities and climate change: An urgent agenda, Rep., World Bank, Washington, D. C.

Xueref-Remy, I., E. Dieudonné, C. Vuillemin, M. Lopez, C. Lac, M. Schmidt, ... & C. Ampe, 2018: Diurnal, synoptic and seasonal variability of atmospheric CO_2 in the Paris megacity area. *Atmos. Chem. Phys.*, **18(5)**, 3335-3362.

Yamato, H., T. Mikami, & H. Takahashi, 2017: Impact of sea breeze penetration over urban areas on midsummer temperature distributions in the Tokyo Metropolitan area. *Int. J. Climatol.*, **37(15)**, 5154-5169.

List of Figures

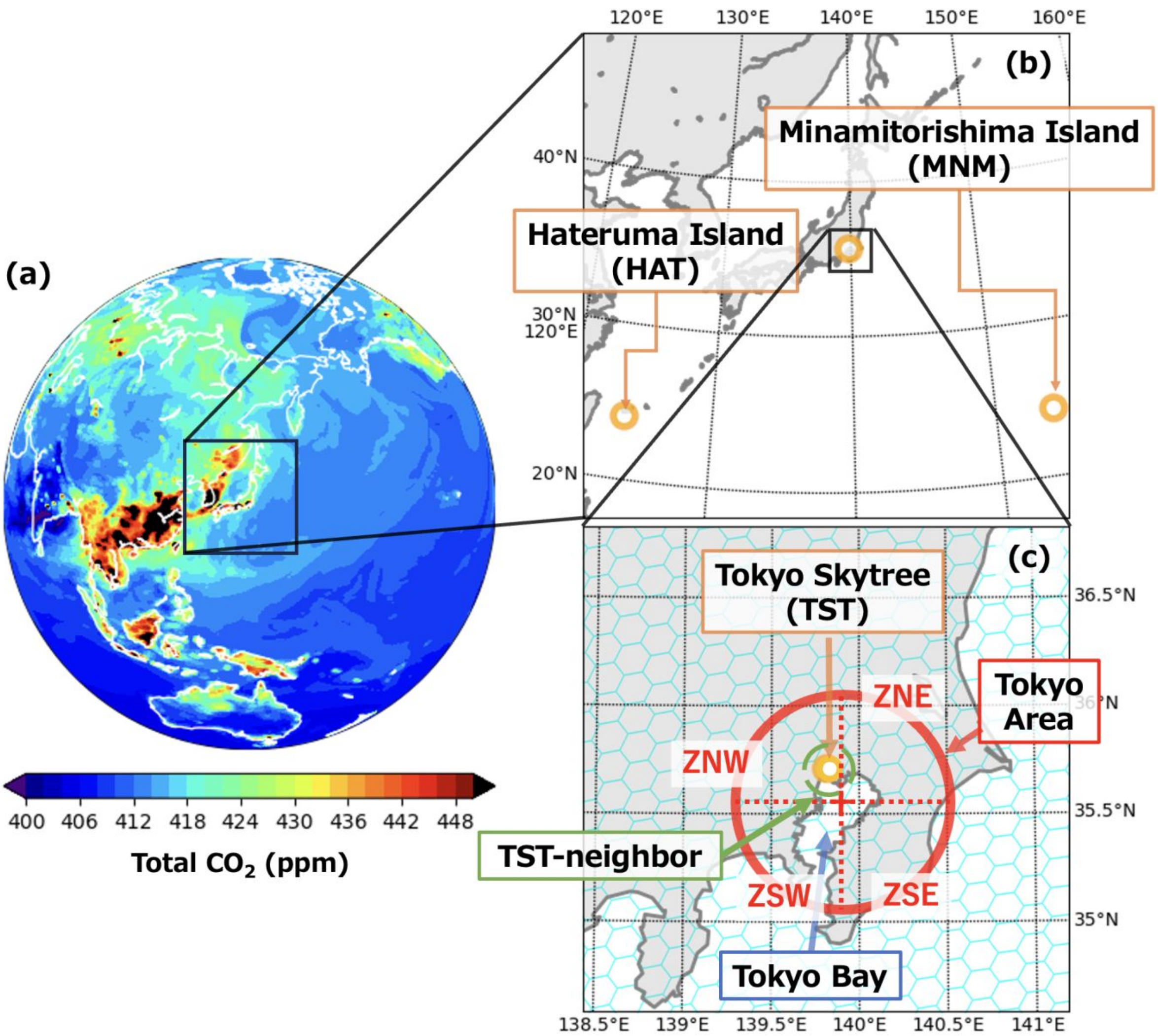

Fig. 1 An example of the NICAM global simulation with glevel-9 (~14 km) resolution for January 15 2019 (a) and analysis regions and target sites (b, c). The red circle in (c) with 50 km radius denotes the Tokyo area as defined in this study, which is separated into four zones. The green circle in (c) around TST indicates TST-neighbor. The cyan hexagons are NICAM grids.

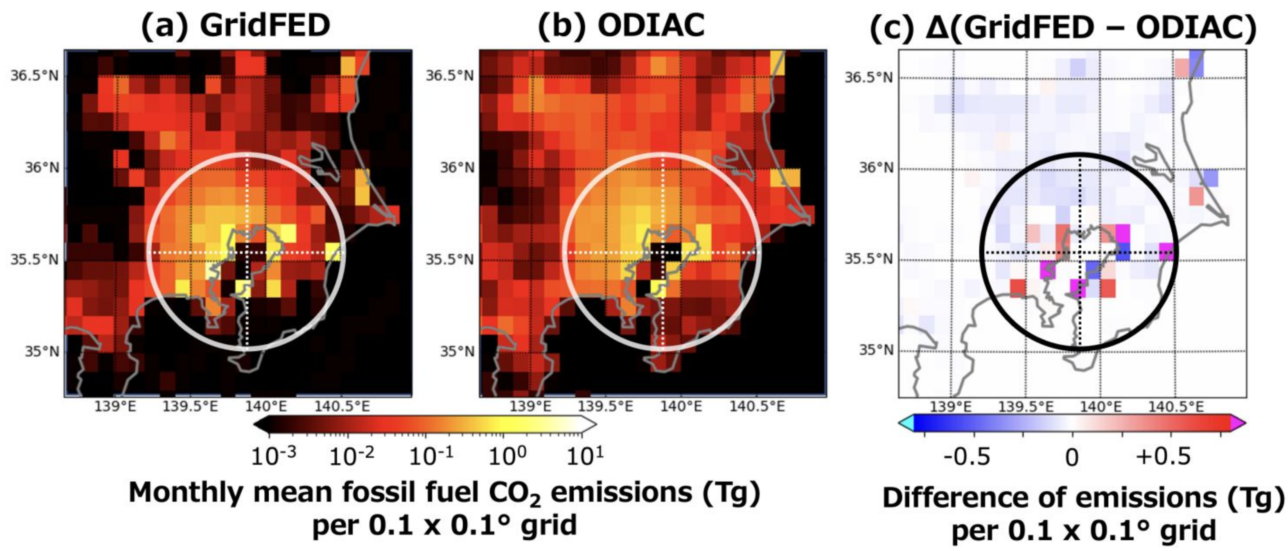

Fig. 2 Distribution of monthly mean fossil-fuel emissions (Tg) per 0.1° grid of (a) GridFED, (b) ODIAC, and (c) the difference between ODIAC and GridFED. ODIAC is averaged from a 0.1 km grid to a 0.1° grid. The circle marks the Tokyo region as shown in Fig. 1c.

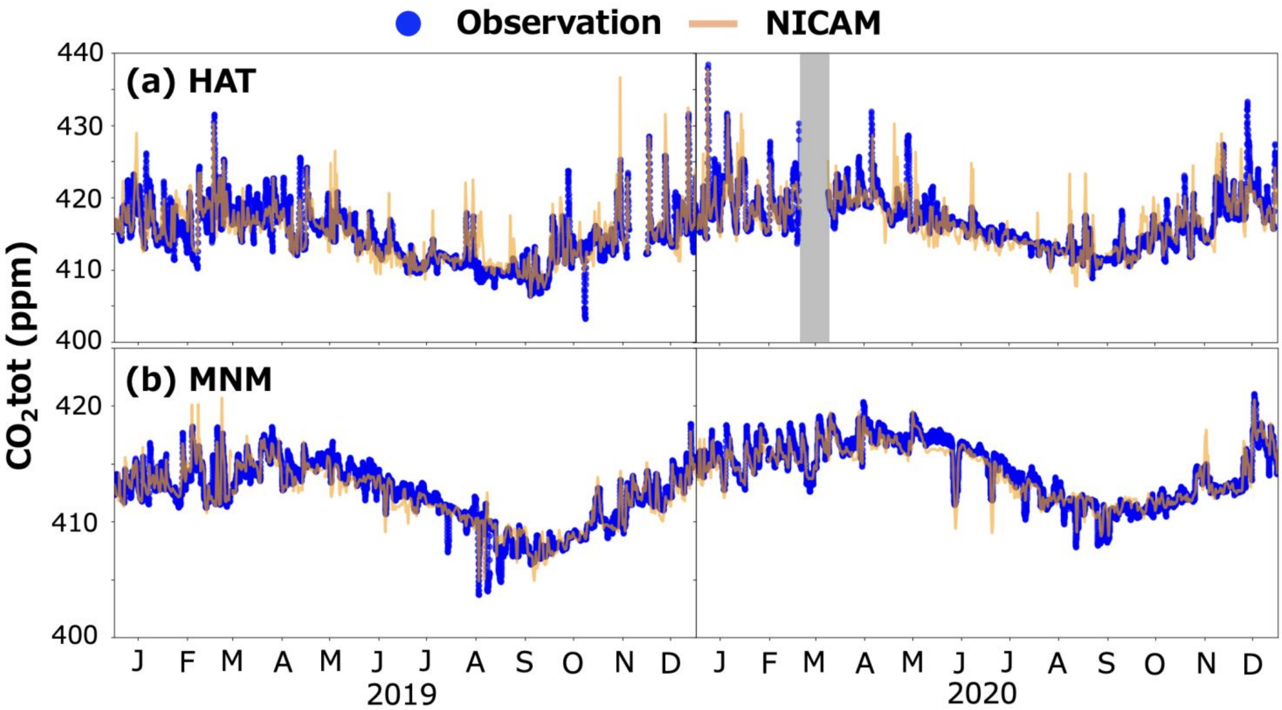

Fig. 3 Observed and NICAM-calculated CO_2tot at (a) Hateruma Island (HAT) and (b) Minamitorishima Island (MNM) for 2019–2020. There were no observations for 5 to 24 March 2020 at HAT.

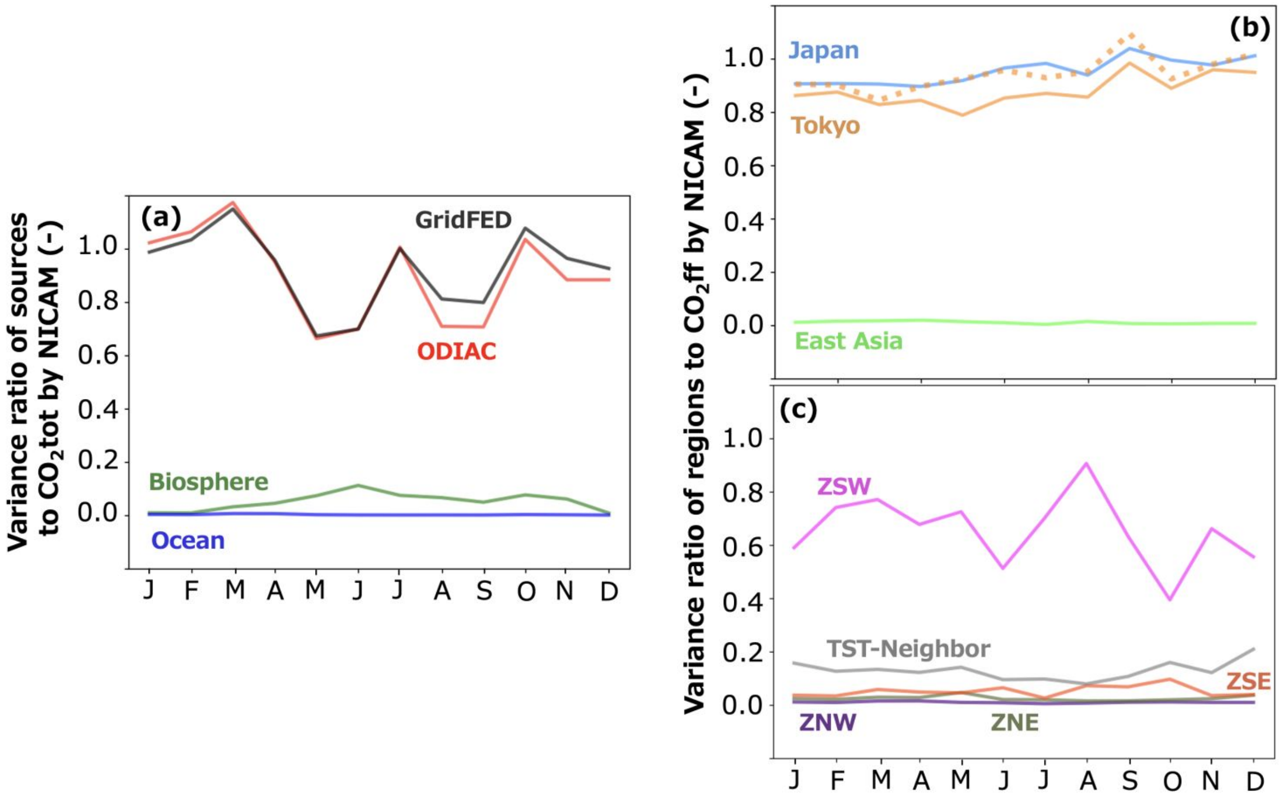

Fig. 4 (a) Monthly means of the variance ratio (VR) of simulated CO_2 concentrations of different source categories to CO_2tot. (b) Monthly means of VR of atmospheric CO_2 concentrations from regionally tagged fossil-fuel emissions of GridFED against those of CO_2ff from GridFED. The dotted orange line indicates CO_2tk. (c) Monthly means of VR of CO_2ff from the four Tokyo zones (shown in Fig. 1c) to CO_2ff from Tokyo calculated by GridFED.

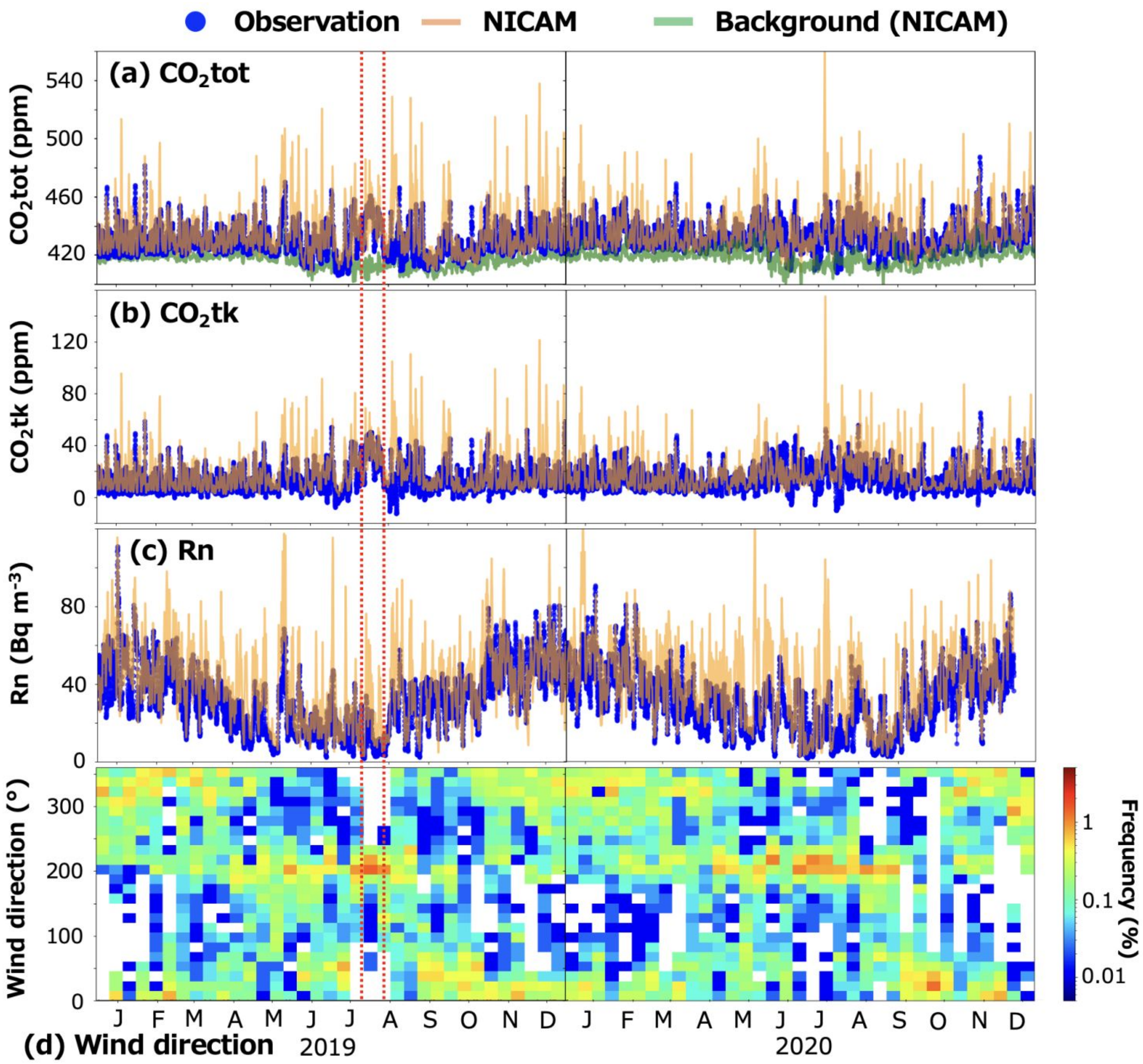

Fig. 5 Observed and NICAM-calculated (a) CO_2tot, (b) CO_2tk, and (c) Rn at TST for 2019–2020. (d) Frequencies of wind direction at TST for 2019–2020. Red dotted lines indicate the high-emissions event caused by the continuous southern wind.

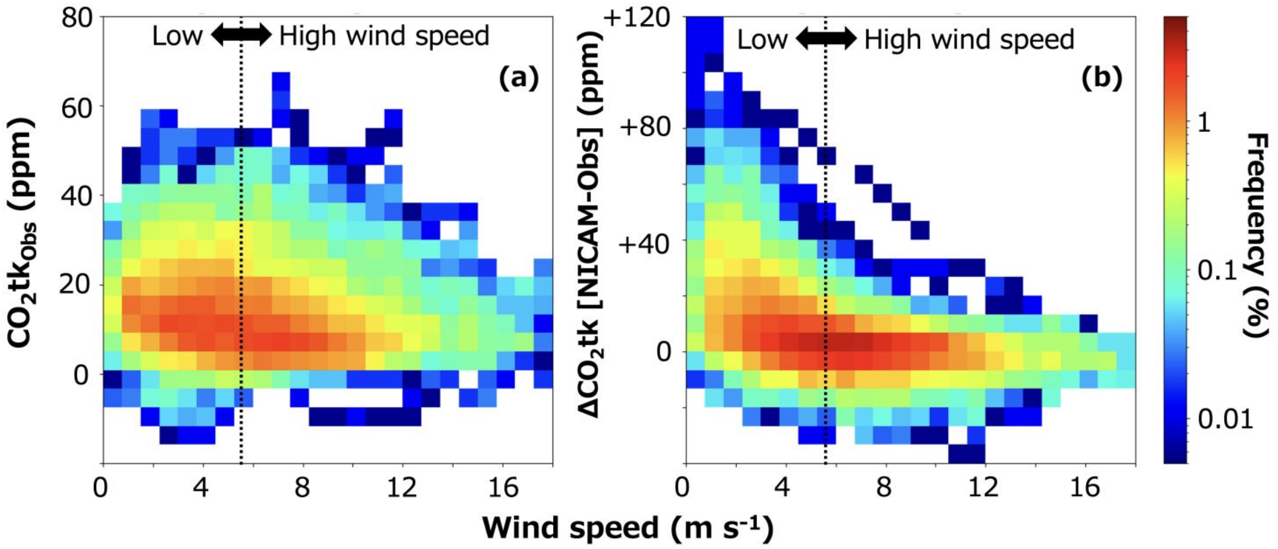

Fig. 6 (a) CO_2tk^{Obs} and (b) the difference between calculated and observed CO_2tk with respect to wind speed.

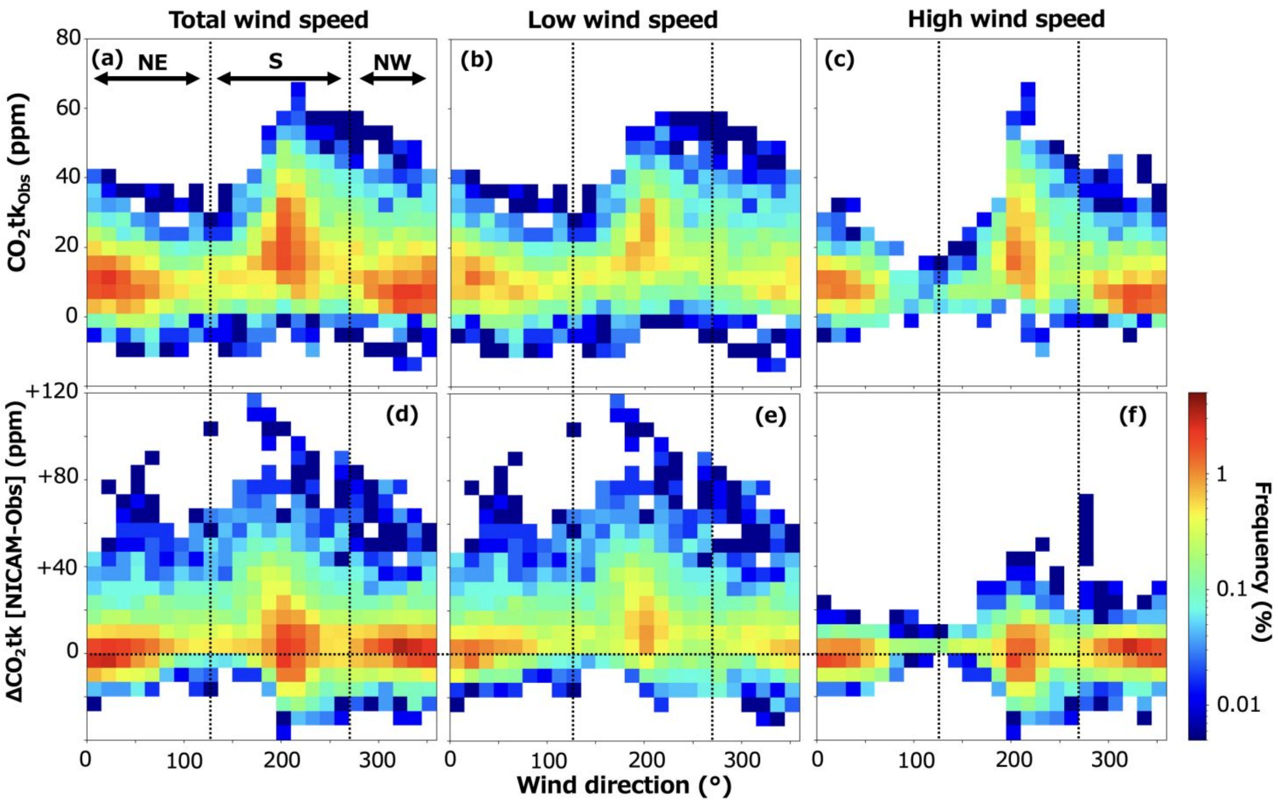

Fig. 7 (a–c) CO_2tk^{Obs} and (d–f) the difference between calculated and observed CO_2tk with respect to wind direction. (a, d) All wind speeds, (b, e) low wind speeds (<5.5 m s^{-1}), (c, f) high wind speeds (>5.5 m s^{-1}).

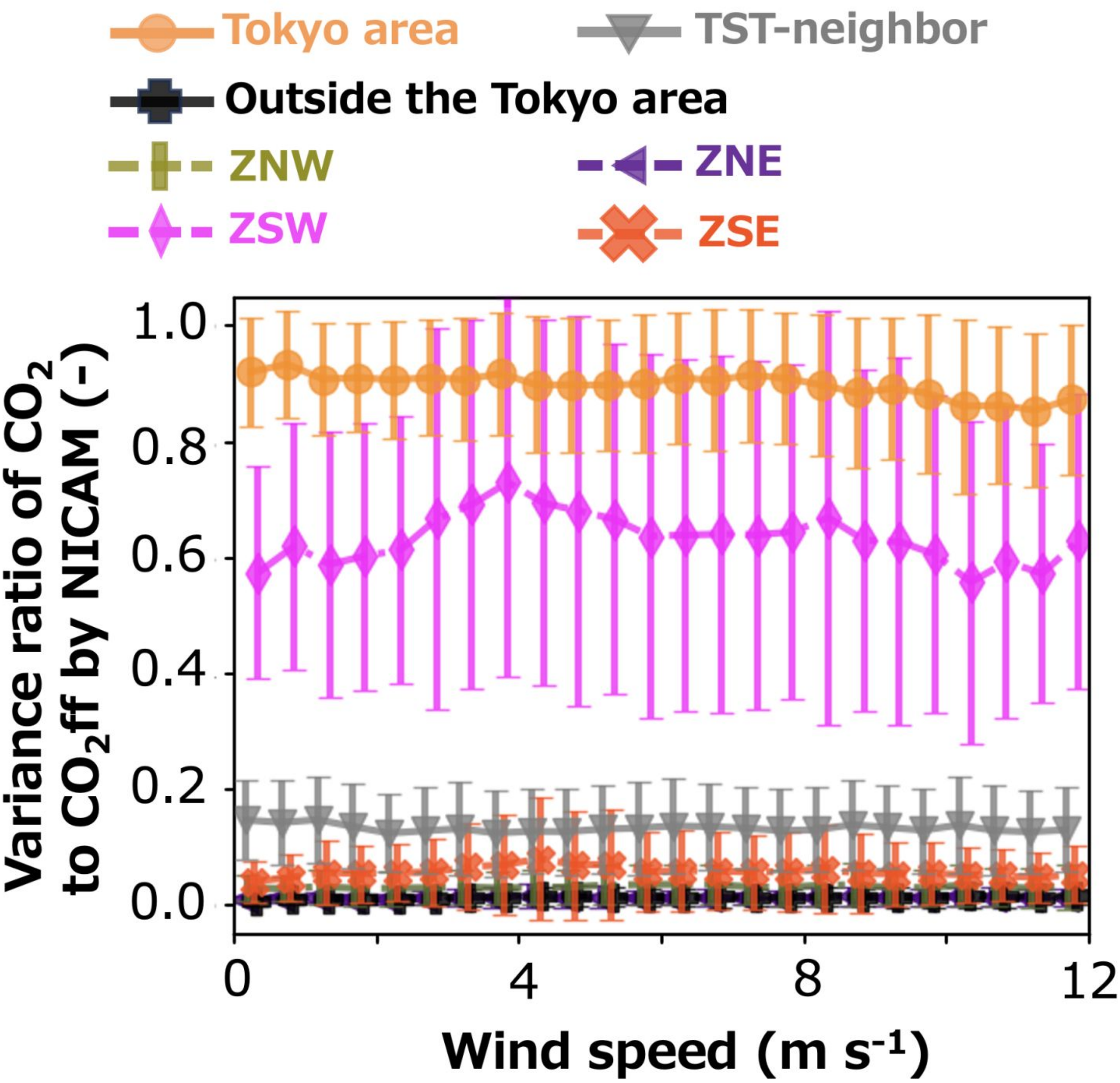

Fig. 8 Variance ratio of CO_2ff from emission regions relative to total CO_2ff for wind-speed classes of 0.5 m s^{-1}. The VR values of ZNE, ZNW, and regions outside the Tokyo area are almost zero. The error bars are the standard deviations.

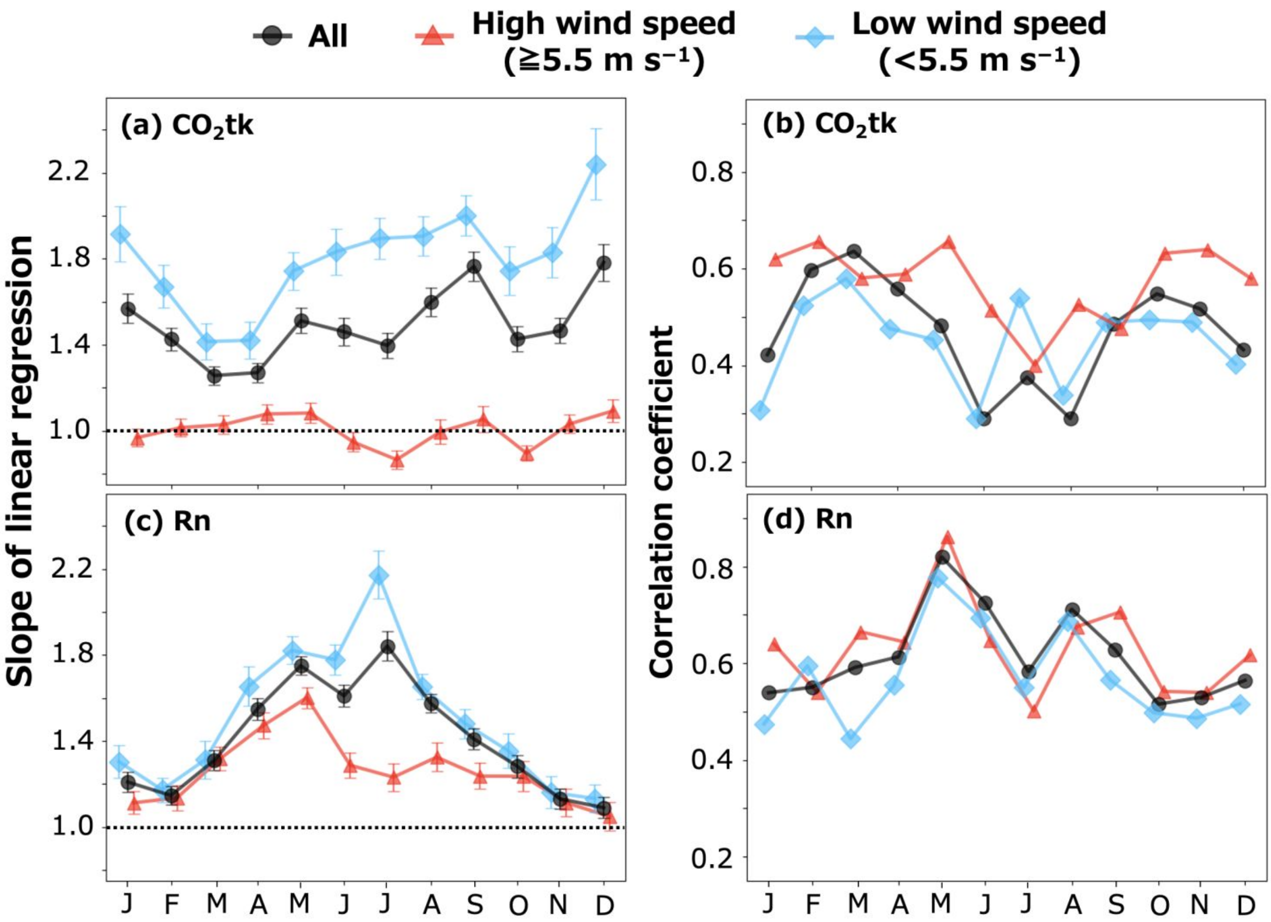

Fig. 9 Mean values of (a) the slope of the linear regression line and (b) the correlation coefficient of CO_2tk between the observations and the NICAM model calculation. Calculations of the regression line and correlation coefficient are for 30-day intervals. The error bars are half of the standard error of the regression slope in (a). (c) and (d) are same as (a) and (b), respectively, but for Rn.

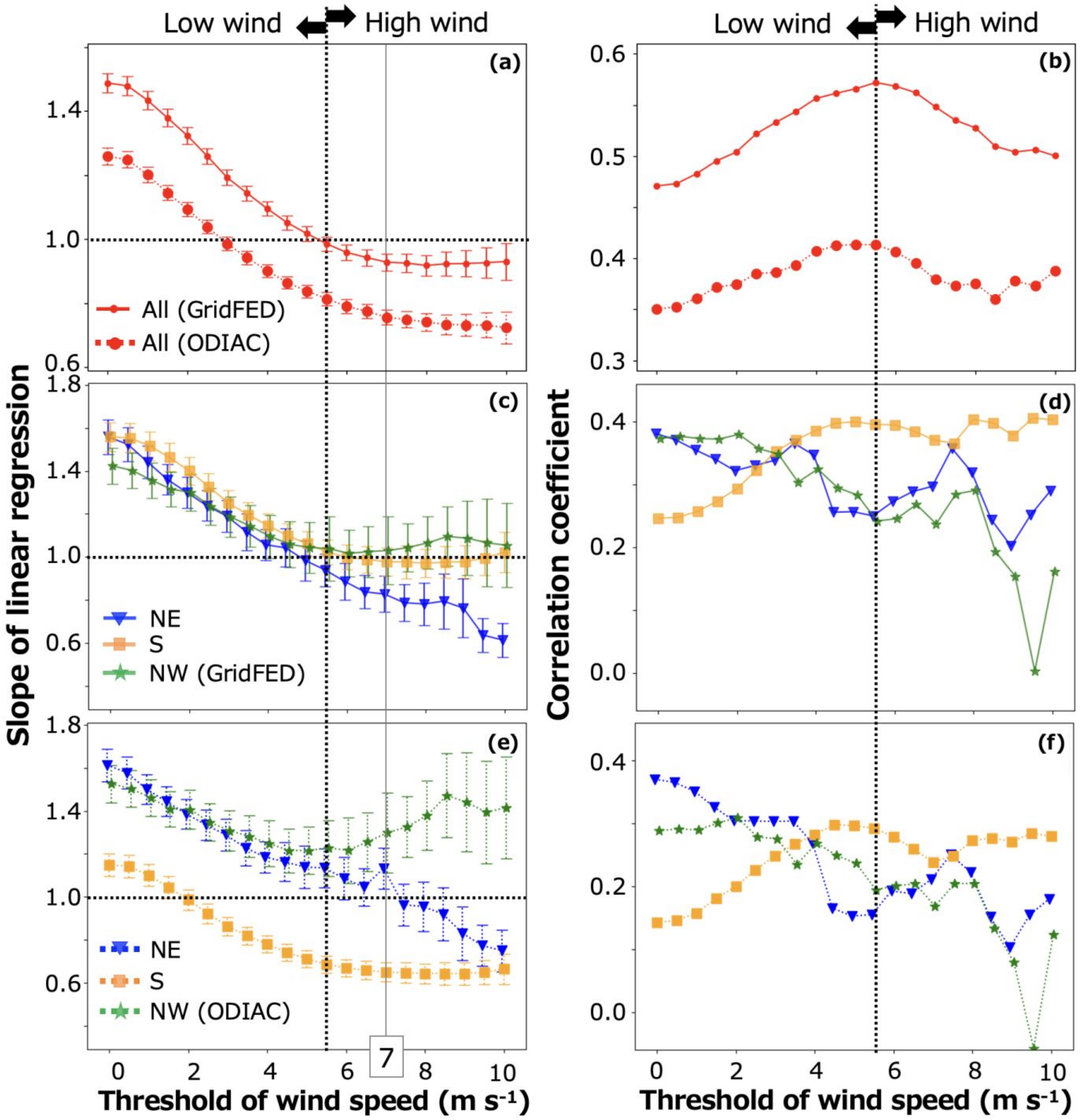

Fig. 10 The slope of the linear regression line with an intercept of zero (a, c, and e) and the correlation coefficient (b, d, and f) between observed and calculated (NICAM model) CO_2tk data for 2019–2020 at TST when wind speeds below the threshold are removed. (a, b) All wind directions and (c, f) separate NE, S, and NW wind directions. c, d show data from GridFED, and e, f show data from ODIAC. The error bars are half of the standard error of the regression slope.

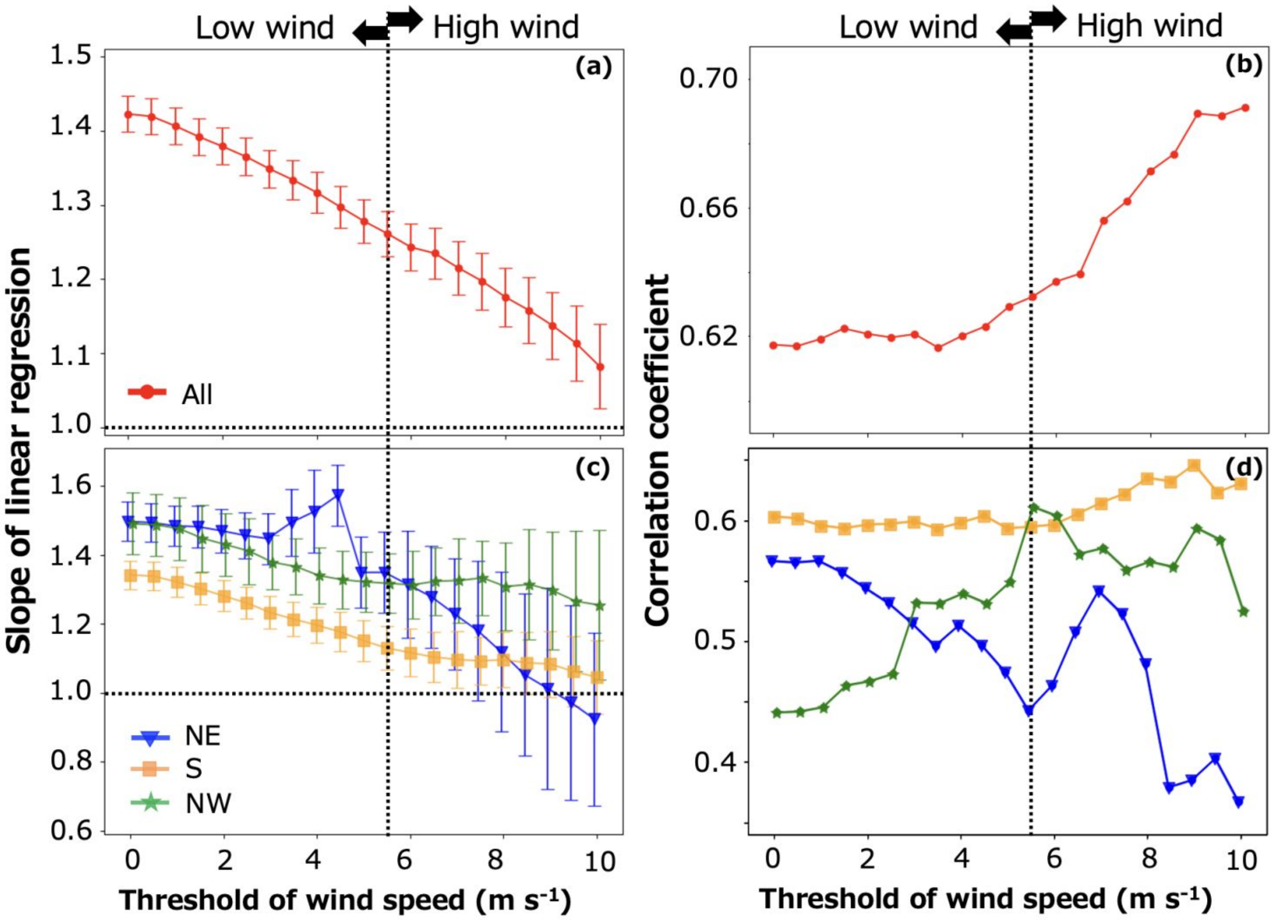

Fig. 11 As Fig. 10, but for Rn.

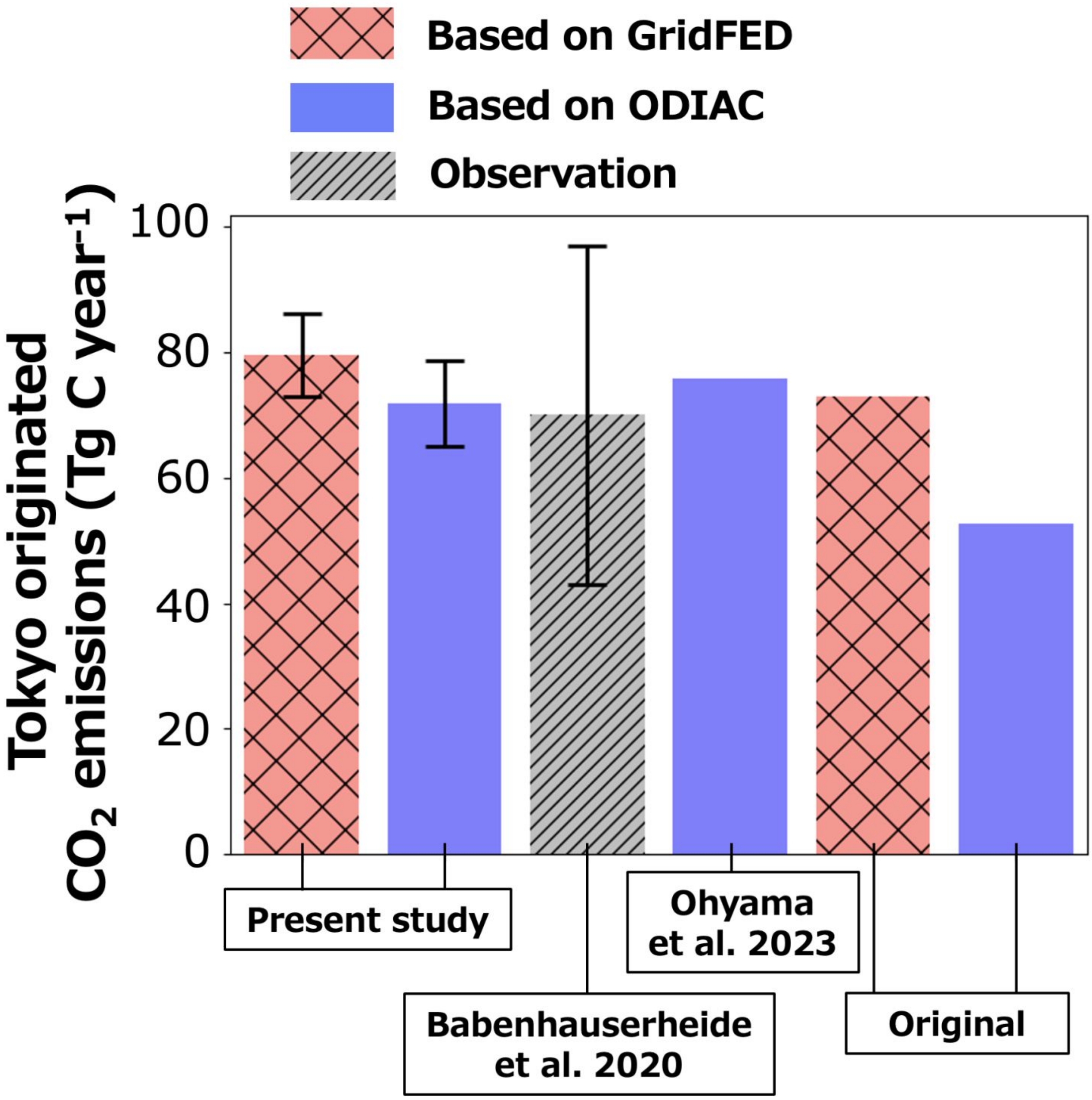

Fig. 12 Comparison of CO_2 emissions from the Tokyo area calculated in this study with the results of Babenhauserheide et al. (2020) and Ohyama et al. (2023). The regions used in the previous studies are different in a strict sense, but similar enough to that in our study.

List of Tables

Type	Value	Reference
Model setting		
Spatial resolution	Glevel-9 (~14km)	
Vertical numbers	40 (vertical resolution < 45 km)	
Turbulence scheme	Mellor-Yamada-Nakanishi-Niino Model	Nakanishi and Niino (2004) Noda et al. (2010)
Cumulus scheme	Chikira-Sugiyama Scheme	Chikira and Sugiyama (2010)
Nudging data	JRA-55 horizontal wind (time constant = 6 h)	Kobayashi et al. (2015)
CO_2 flux data		
Fossil fuel	GridFED ODIAC	Jones et al. (2021) Oda et al. (2018)
Biosphere	VISIT	Ito (2019)
Air-sea	JMA air-sea CO_2 flux data	Iida et al., (2021)
Biomass burning	GFED	van der Werf et al. (2017)

JRA-55: The Japanese 55-year Reanalysis project
GridFED: The Global Carbon Budget Gridded Fossil Emissions Dataset
ODIAC: The Open-Data Inventory for Anthropogenic Carbon dioxide
VISIT: The Vegetation Integrative SImulator for Trace gases
JMA: Japan Meteorological Agency
GFED: The Global Fire Emissions Database

Table 1: Settings used for the NICAM model.